Plasmonic response of complex nanoparticle assemblies

Zachary M. Sherman,[†] Kihoon Kim,[†,§] Jiho Kang,[†,§] Benjamin J. Roman,[†] Hannah S. N. Crory,[‡] Diana L. Conrad,[‡] Stephanie A. Valenzuela,[‡] Emily Y. Lin,[†] Manuel N. Dominguez,[‡] Stephen L. Gibbs,[†] Eric V. Anslyn,[*,‡] Delia J. Milliron,[*,†,‡] and Thomas M. Truskett[*,†,¶]

[†]McKetta Department of Chemical Engineering, University of Texas at Austin, Austin, 78712, Texas, United States

[‡]Department of Chemistry, University of Texas at Austin, Austin, 78712, Texas, United States

[¶]Department of Physics, University of Texas at Austin, Austin, 78712, Texas, United States

[§]These authors contributed equally to this work.

E-mail: anslyn@austin.utexas.edu; milliron@che.utexas.edu; truskett@che.utexas.edu

Abstract

Optical properties of nanoparticle assemblies reflect the distinctive characteristics of their building blocks and their spatial organization, giving rise to emergent phenomena. Integrated experimental and computational studies have established design principles connecting structure to properties for assembled clusters and superlattices. However, conventional electromagnetic simulations are too computationally expensive to treat more complex assemblies. Here we establish a fast, materials agnostic method to simulate the optical response of large nanoparticle assemblies incorporating both structural

1

and compositional complexity. This many-bodied, mutual polarization method resolves limitations of established approaches, achieving rapid, accurate convergence for configurations including thousands of nanoparticles, some overlapping. We demonstrate these capabilities by reproducing experimental trends and uncovering far- and near-field mechanisms governing the optical response of plasmonic semiconductor nanocrystal assemblies, including structurally complex gel networks and compositionally complex mixed binary superlattices. This broadly applicable framework will facilitate design of complex, hierarchically structured, and dynamic assemblies for desired optical characteristics.

The tunable optical response of plasmonic nanoparticle assemblies makes them attractive for applications including sensing,[1,2] energy conversion,[3–5] and theranostics.[6,7] Developing and employing methods for electrodynamics simulation of metallic nanoparticle assemblies are essential for advancing conceptual understanding and design. The resonant interaction of free charge carriers in nanoparticles with light (localized surface plasmon resonance, LSPR) results in strong electromagnetic near-fields and enhanced absorption and scattering.[8,9] Due to LSPR coupling, the spectral response of plasmonic assemblies is sensitive to the nanoparticle spatial arrangement, i.e., structure, with amplified electromagnetic fields or hot spots emerging in the gaps between closely spaced nanoparticles.[10–13] Analytical approaches such as Mie theories[14] or plasmon hybridization theory[11,15] and numerical solution of the classical electromagnetic scattering equations[10–12,16–21] have clarified the influence of nanoparticle morphology and coupling in small plasmonic clusters, oligomers, and periodic arrays. However, an open question is how to compute the optical response of significantly more complex assemblies with characteristic structural features involving large numbers of nanoparticles, such as compositionally disordered superlattices[22–24] or gel networks.[13,25–29]

Structural complexity of extended, disordered nanoparticle assemblies poses challenges for conventional electromagnetic simulation techniques. Discretization requirements for the most flexible approaches—discrete dipole approximation, finite difference time domain, finite element, and boundary element methods[19,20]—render them too

computationally demanding to simulate configurations with a large number N $(> 10^3)$ of nanoparticles. This shortcoming can be avoided for assemblies of spherical nanoparticles using strategies like the multisphere T-matrix method,[30–34] which is based on generalized Mie theory[14] and does not require spatio-temporal discretization. However, even these approaches become slow to converge or fail altogether when nanoparticle pairs touch or overlap, which inevitably occurs in large configurations generated from simulations of assembly using coarse-grained models. The ability to predict the optical response of complex assemblies, including those from simulated nanoparticle configurations, is needed to match the complexity of emerging experimental systems[22–24,26,27] and accelerate their development.

Building on a framework from electrostatics, here we establish a mutual polarization method (MPM) capable of rapidly simulating the frequency-dependent optical response of large, complex assemblies of spherical nanoparticles with arbitrary dielectric functions (Fig. 1), accommodating configurations with particle overlaps and triply periodic boundary conditions. We use this approach to predict and interpret experimental spectra for disordered systems with characteristic features that comprise more nanoparticles than would be practical to analyze by conventional electromagnetic simulations: 1) two-dimensional randomly mixed binary superlattices and 2) three-dimensional nanoparticle gel networks. Our analysis shows how far-field spectral features emerge from heterogeneous, structure-dependent near-field coupling and illustrates how MPM helps integrate data from structural and optical measurements to provide insights about ordering across length scales in complex assemblies.

Mutual Polarization Method

MPM computes the optical response based on the polarization of each particle by the applied field $\mathbf{E}_0$ and by the electric dipoles of the other $N - 1$ particles in the system. The polarization depends on the particle's composition as reflected by its dielectric function $\varepsilon_i(\omega)$, where ω is the frequency of light. Spherical particles of any
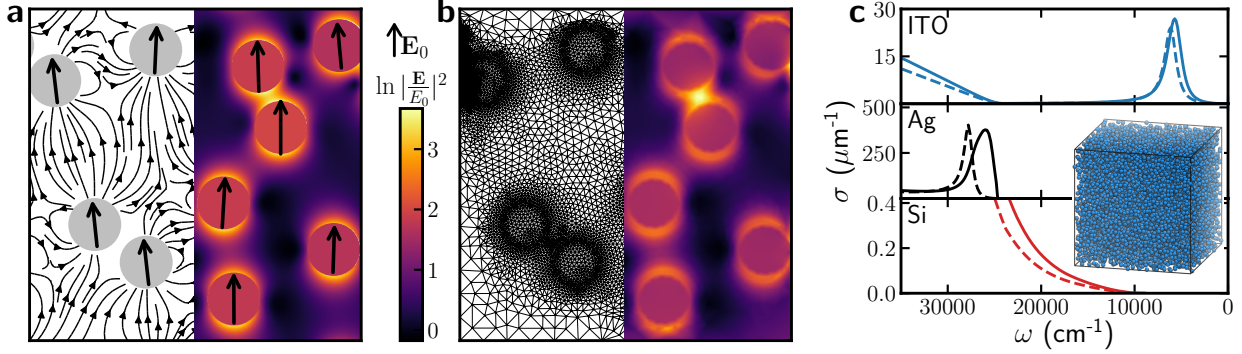
3

Figure 1: **Broad applicability of MPM.** Schematic illustrations and resultant electric field maps generated using (**a**) MPM and (**b**) finite element methods for ITO nanocrystals at area fraction of 0.20. (**c**) Calculated extinction coefficients for dilute (dashed lines) and concentrated (volume fraction 0.20, solid) dispersions of ITO, silver, and silicon nanoparticles using MPM with the dielectric functions shown in Table S3. Coupling redshifts and broadens the LSPR peaks for silver and ITO at high concentration (configuration shown in inset).

dielectric function can be treated (Fig. 1c), however here we only consider particles in the quasistatic limit, where their radius a is small compared to the wavelength of light. This simplification is broadly applicable for LSPR coupling in nanoparticle assemblies, and it allows the $3N$ particle dipole moment components $\mathbf{p}_1, \ldots, \mathbf{p}_N$ to be determined by solving the electrostatics limit of Maxwell's equations, i.e., the Poisson and Laplace equations.

Like other approaches based on generalized Mie theory,[14] MPM does not require fine spatial discretization to solve the electromagnetic scattering problem, though its predictions compare favorably with those from finite element solutions (Fig. 1b and S1-S3). MPM neglects multipole moments induced by local field gradients, yet it captures all significant structure-dependent trends in the far- and near-field optical response. As a result, MPM can compute the optical response of assemblies with more complex structures involving large particle numbers.

Once the electric dipole for each particle i is determined from MPM, the local electric field $\mathbf{E}(\mathbf{x})$ can be computed at any position $\mathbf{x}$. A sum of the incident field and the fields of the scattered waves, it can be expressed (to lowest order in ω) as $\mathbf{E}(\mathbf{x}) = \mathbf{E}_0 + \sum_i^N (4\pi\varepsilon_{\mathrm{m}} r^3)^{-1} (3\hat{\mathbf{r}}\hat{\mathbf{r}} - \mathbf{I}) \cdot \mathbf{p}_i$, where $\mathbf{r} = \mathbf{x} - \mathbf{x}_i$, $\mathbf{x}_i$ is particle i's position,

4

$r = |\mathbf{r}|$, $\hat{\mathbf{r}} = \mathbf{r}/r$, $\mathbf{I}$ is the identity tensor, and ε_{m} is the (real and frequency-independent) permittivity of the medium. Particle i's dipole can be further expressed in terms of the local field, $\mathbf{p}_i = \varepsilon_{\mathrm{m}}\alpha_i(\omega)\mathbf{E}(\mathbf{x}_i)$, where $\alpha_i(\omega) = 4\pi a^3[\varepsilon_i(\omega) - \varepsilon_{\mathrm{m}}]/[\varepsilon_i(\omega) + 2\varepsilon_{\mathrm{m}}]$ is the dipolar polarizability. Other observables related to the optical response—such as frequency-dependent extinction coefficient σ or transmittance through a nanoparticle film—can be readily computed from these quantities using Maxwell's equations (Supporting Information Sec. 1.2 and 4.2).

The heart of the many-body MPM computation is efficient solution of the linear system of equations for the N particle dipoles,

$$\mathbf{E}_0 = \sum_{j}^{N} \mathbf{M}_{ij} \cdot \mathbf{p}_j \tag{1}$$

Here, we have introduced a scattering matrix with elements $\mathbf{M}_{ij}$,

$$\mathbf{M}_{ij} = \begin{cases} \dfrac{1}{\varepsilon_{\mathrm{m}}\alpha_i}\mathbf{I} & i = j \\[2ex] \dfrac{1}{4\pi\varepsilon_{\mathrm{m}}r_{ij}^3}\left(\mathbf{I} - 3\hat{\mathbf{r}}_{ij}\hat{\mathbf{r}}_{ij}\right) & i \neq j, r_{ij} \geq 2a \\[2ex] \dfrac{1}{4\pi a^3\varepsilon_{\mathrm{m}}}\left[\left(1 - \dfrac{9r_{ij}}{16a} + \dfrac{r_{ij}^3}{32a^3}\right)\mathbf{I} + \left(\dfrac{3r_{ij}^3}{32a^3} - \dfrac{9r_{ij}}{16a}\right)\hat{\mathbf{r}}_{ij}\hat{\mathbf{r}}_{ij}\right] & i \neq j, r_{ij} < 2a \end{cases}, \tag{2}$$

constructed to avoid singularities, unphysical property predictions, and convergence problems when solving for the dipoles (Fig. S4 and S5) due to particles with overlapping optical cores ($r_{ij} < 2a$). Overlaps can naturally occur in large configurations of simulated assemblies due to coarse-grained model nanoparticle interactions, but this scattering matrix is readily inverted to obtain well-behaved solutions of eq 1 for any spatial arrangement of the particles. Similar regularization strategies have been applied to treat overlaps while simulating other physical phenomena, e.g., many-bodied hydrodynamic[35,36] and magnetic[37,38] interparticle forces in colloidal suspensions, which require assigning sharp particle interfaces (for continuum property modeling) together with soft-particle interactions (for dynamics). For triply-periodic geometries, $\mathbf{M}_{ij}$ can be expressed in a compact form (eq S3) amenable to a highly efficient, spectrally accu-

rate Ewald summation method [39] that allows the linear system for dipoles to be solved

efficiently using the generalized minimal residual method (GMRES). [40] Our implemen-

tation of MPM is publicly available (see Methods).
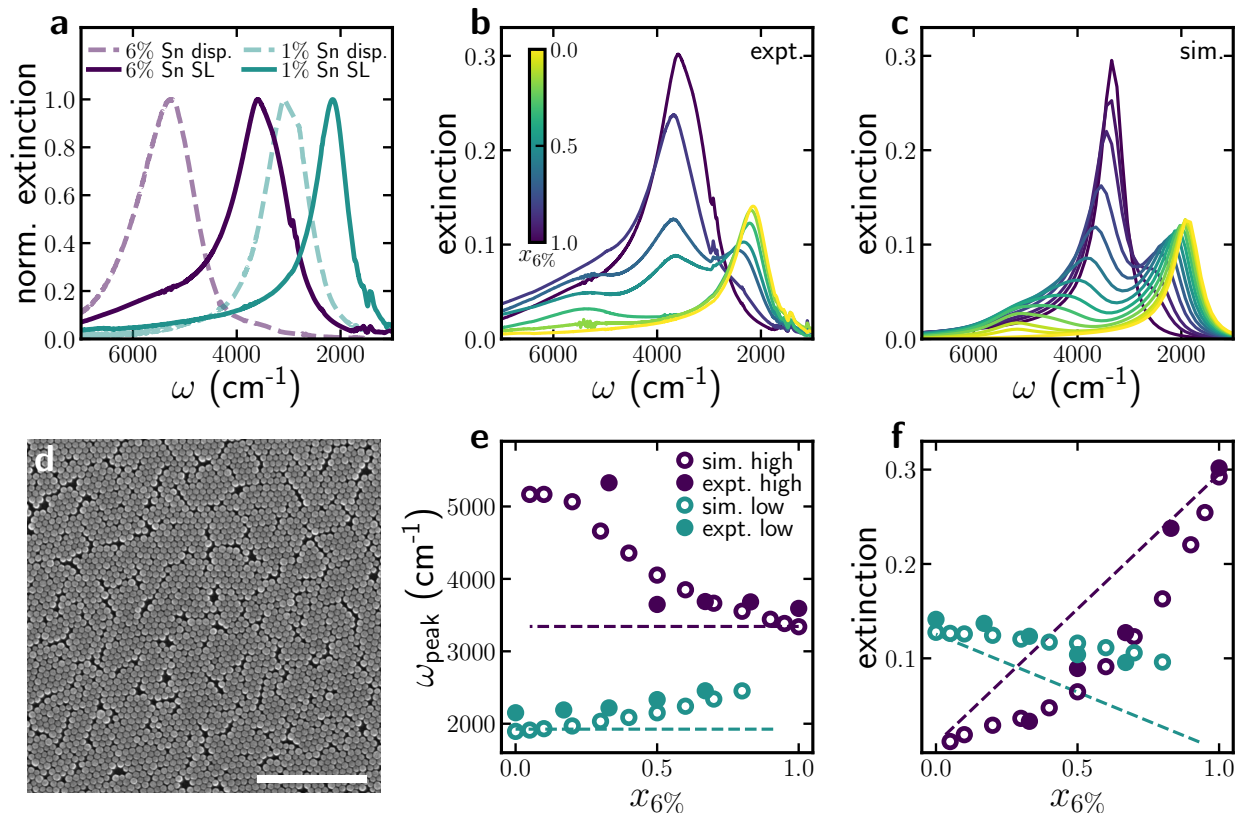
Mixed Nanocrystal Superlattices

Figure 2: **Spectral response of mixed ITO nanocrystal superlattices.** (**a**) Experimental extinction spectra for nanocrystal dispersions (dashed) and single-component superlattices (solid). (**b**) Experimental and (**c**) simulated extinction spectra for various compositions $x_{6\%}$ of mixed superlattices. (**d**) Scanning electron micrograph of a mixed superlattice comprising 1% Sn and 6% Sn ITO nanocrystals (scale bar 500 nm). (**e**) Extinction peak locations ω_{peak} and (**f**) heights from **b** and **c** as a function of $x_{6\%}$. The dashed lines indicate the values that would result from simple linear mixing of the pure 6% and pure 1% superlattice spectra.

To demonstrate the utility of MPM for design of compositionally complex nanoparticle assemblies we analyze the collective optical response of mixed nanocrystal superlattices, where the mixing ratio allows continuous tuning of effective properties. Tin-

6

doped indium oxide (ITO) nanocrystals have a near-ideal metallic dielectric function with a tunable LSPR depending on the chosen dopant concentration (% Sn). Consistent with previous reports of other nanocrystal compositions,[22–24] we found that ITO nanocrystals with different % Sn readily form intermixed two-dimensional hexagonal superlattices, as long as their sizes are closely matched (here, $a \approx 15$ nm, Fig. 2d, S6, and S7).

At infrared wavelengths, the ITO permittivity is well-described by a simple Drude dielectric function:

$$\varepsilon_p(\omega) = \varepsilon_\infty - \frac{\varepsilon_0 \omega_p^2}{\omega^2 + i\gamma\omega} \tag{3}$$

where ε_∞ is the high-frequency permittivity, set equal to $4\varepsilon_0$, while doping changes both ω_p, that primarily controls the LSPR peak position, and γ that determines peak width. Plasmonic coupling causes a large redshift of the extinction spectrum upon assembly into a superlattice (Fig. 2a). However, when scaled by ω_p, the magnitude of this shift is independent of % Sn (Table S1). In this sense, the range of attainable optical responses is limited for single-component superlattices, even when the nanocrystal building blocks themselves have continuously tunable properties.

Although binary superlattices with ordered arrangements of two components[41,42] are difficult to assemble experimentally, they are simple to study computationally because they can be modeled using a small periodic unit cell. Conversely, randomly mixed superlattices are computationally challenging; a large number of particles must be used to prevent periodic boundary conditions imposing artificial sublattice ordering and to adequately sample the possible nanocrystal arrangements.

We vary the mixing ratio of 1% Sn and 6% Sn ITO nanocrystals in superlattices continuously, changing the fraction of 6% Sn nanocrystals, $x_{6\%}$, from 0 to 1. Qualitatively, the normal incidence extinction spectra of the mixed superlattices evolve systematically between the spectra of the two single-component assemblies, but neither the peak positions nor the heights reflect simple linear mixing (Fig. 2b). Electron transfer is not expected to occur between nanocrystals,[43] but LSPR coupling between

7

neighboring nanocrystals should depend on their % Sn.

These spectral trends are accurately reproduced in simulations of superlattice extinction using MPM (Fig. 2c). We model the superlattices by constructing 2D hexagonal lattices containing 11600 nanocrystals, each having one of two Drude dielectric functions using parameters (ω_p and γ) determined by fitting the extinction spectra of dilute solvent dispersions of the corresponding nanocrystals (Fig. S8 and Table S2).[44] Using MPM, we simulate the normal incidence extinction spectra, averaged over 2 polarizations and 20 superlattices independently prepared by randomly arranging the nanocrystals. The correspondence with the experimental spectra supports our supposition that the lattices are well-mixed, with little to no phase segregation between the two types of ITO nanocrystals, an outcome that would be difficult to directly verify by electron microscopy owing to their very similar electron densities.

As such, we interpret the shifting peak positions with composition ($x_{6\%}$) as arising from a changing average number of spectrally resonant neighboring nanocrystals (Fig. 2e). For instance, compared to a pure 1% Sn superlattice ($x_{6\%} = 0$), the lower frequency extinction peak blueshifts with increasing $x_{6\%}$ as each 1% Sn nanocrystal has fewer 1% Sn neighbors with which to couple. The same is true of the higher frequency peak moving away from $x_{6\%} = 1$. A third peak, around $5100\,\mathrm{cm}^{-1}$, arises only for intermediate compositions, ascribed to "isolated" 6% Sn nanocrystals with relatively few 6% Sn neighbors.

To understand the trends in peak heights (Fig. 2f) requires microscopic insight made possible by visualizing the spatial variation of the dipolar polarizations and the resulting local electric fields (Fig. 3) and quantifying their probability distributions (Fig. S9). For instance, starting from $x_{6\%} = 1$, the intensity of the high frequency peak drops much more quickly with changing $x_{6\%}$ than would be expected from linear mixing. For a superlattice containing a fraction $x_{6\%} = 0.80$ of 6% Sn nanocrystals, examining the dipoles induced by excitation at the peak, we find that the 1% Sn nanocrystals are effectively acting as dielectric spacers that have minimal polarization, so 6% Sn nanocrystals near 1% Sn nanocrystals have significantly reduced dipoles because they

8

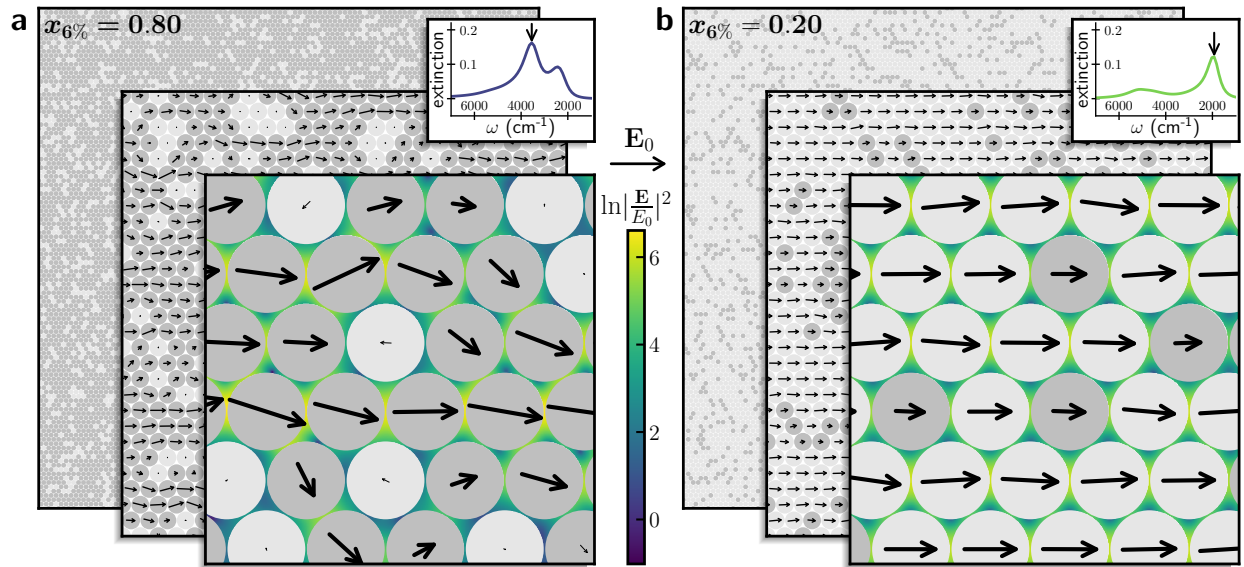Figure 3: **Electric near-field maps for mixed nanocrystal superlattices.** Spatial maps of the local field intensity at (**a**) the high-frequency LSPR for $x_{6\%} = 0.80$ and (**b**) the low-frequency LSPR for $x_{6\%} = 0.20$. Foreground panels magnify small areas within the entire simulated configuration shown in the backmost panel. Dark (6% Sn) and light (1% Sn) gray indicate the nanocrystal type, arrow lengths indicate the magnitude and direction of the imaginary part of each particle's dipole moment. Corresponding extinction spectra are inset with the excitation frequency indicated.

do not get a mutual polarization boost (Fig. 3a). These effects weaken the overall response, reducing the extinction intensity. The field is also highly concentrated along the paths formed by 6% Sn nanocrystals, resulting in a heterogeneous distribution of field strengths and dipole orientations (Fig. S9). In a superlattice with only a fraction $x_{6\%} = 0.20$ of 6% Sn nanocrystals, conversely, the 1% Sn nanocrystals' polarization is enhanced by coupling to neighboring 1% Sn and 6% Sn nanocrystals alike, strengthening and better aligning their dipoles with the applied field (Fig. 3b). As a result, the low frequency extinction peak intensity falls off more gradually than expected from linear mixing as $x_{6\%}$ increases, and the local field enhancement is more evenly distributed (Fig. S9). The spectral redistribution of extinction and spatial redistribution of electric field intensity hint at a rich variety of effective metamaterial properties and near-field phenomena that could be realized in mixed nanocrystal superlattices. MPM's ability to rapidly screen a large compositional parameter space will be enabling in the exploration of these possibilities.

Nanocrystal Gels

Nanocrystal gels have structural complexity that spans length scales, which has so far hampered the use of simulations to predict or rationalize their structure-dependent optical properties. Although plasmonic nanoparticle gels have been reported to exhibit spectrally shifted and broadened extinction spectra compared to their constituent nanoparticles, these effects vary widely and unpredictably for different nanoparticle compositions and gel preparation strategies.[13,25–27] We demonstrate the value of MPM for understanding gel structure and optical properties by considering networks of ITO nanocrystals ($a \approx 6\,\mathrm{nm}$, 6.0% Sn) linked by dynamic covalent bonding[26] (Fig. 4, S10, and S11).

Gel structure commonly depends on sample history and preparation protocol, and we find that the structure factor S acquired by small-angle X-ray scattering (SAXS) of ITO nanocrystal gels evolves systematically with the amount of the non-coordinating
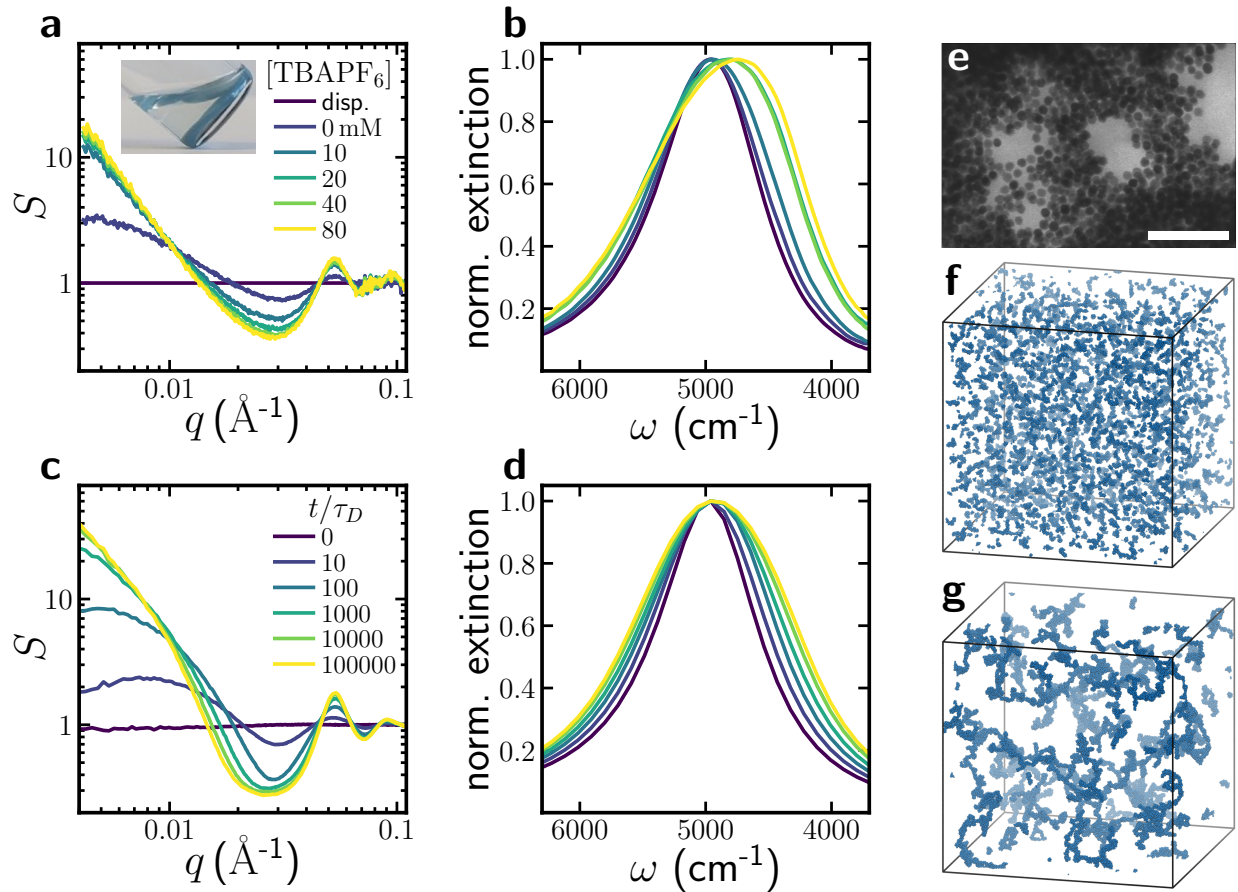
10

Figure 4: **Structural and optical evolution of ITO nanocrystal gels.** (**a**) Experimental SAXS stucture factors S (gel seen in blue, photo inset) and (**b**) extinction spectra of a dispersion and gels 11 days after preparation. Simulated (**c**) S and (**d**) extinction spectra. (**e**) Scanning transmission electron micrograph of a gel (scale bar, 100 nm). Simulation snapshots at coarsening times (**f**) $t = 1000\tau_D$ and (**g**) $100000\tau_D$.

salt, tetrabutylammonium hexafluorophosphate (TBAPF$_6$), present during gel formation (Fig. 4a and S12). The enhancement of the primary peak at wavenumber $q \sim 0.05\,\text{Å}^{-1}$ and progressive deepening of the minimum at lower q are reminiscent of coarsening,[45] suggesting the salt concentration determines the extent of structural evolution approaching arrest. These features are replicated in Brownian dynamics simulations of coarsening of nanoparticles with strong, short-ranged attractions (Fig. 4c,f,g and S13. Indeed, the S at higher [TBAPF$_6$] superposes with S for a lower [TBAPF$_6$] gel at longer aging time, supporting a correspondence between the effects of salt concentration and time (Fig. S14). However, other structures, like cluster fluids of varying cluster fractal dimension, can have similar S, so S alone is not sufficient to determine the microstructural evolution (Fig. S15).

The optical extinction spectra of the gels also depend on salt concentration (Fig. 4b), providing complementary information to help understand their structures. At higher [TBAPF$_6$], the extinction broadens and redshifts. We use MPM to test whether coarsening can explain these changes. ITO nanocrystals in this size range are known to have a radially varying free electron concentration, so we model their dielectric function with a Drude-type plasmonic core and a dielectric shell, complexity easily incorporated into MPM. As before, the parameters describing the dielectric function are determined by fitting the LSPR spectrum of a dilute nanocrystal dispersion (Fig. S8, Tables S2 and S3).[44] At each of six stages of coarsening from the Brownian dynamics trajectory, we use MPM to compute the polarization-averaged extinction spectrum for the 64000-nanoparticle configuration (Fig. 4d). The simulations reproduce the asymmetric broadening observed experimentally, while other candidate microstructures like cluster fluids with similar trends in S show the opposite optical broadening trends (Fig. S15). However, the local density increases much more, by over an order of magnitude, during coarsening (Fig. S16), drastically changing the dipolar coupling environment and instigating the optical broadening. This example illustrates the power of MPM to combine structural and optical information to provide mechanistic insights across length scales in structurally complex assemblies.

Outlook

Building on advances presented here, MPM's computational efficiency will enable on-the-fly evaluation of optical properties in dynamic, nanoparticle-based simulations, making possible the design of complex plasmonic assemblies with targeted near- or far-field responses using inverse methods.[46] Computation-guided design of disordered structures with desired optical properties is particularly compelling for soft hybrid materials, e.g., plasmonic gels[13,25–27] that can dynamically reconfigure—modulating how they interact with light—in response to stimuli. In design of hybrid materials, MPM can readily compute optical properties for networks comprising both dielectric (e.g., semiconductor) and metal nanoparticles or with hierarchical nanoparticle ordering, significantly expanding the design space where computation can enhance experimental discovery. An intriguing possibility is the creation of plasmonic materials with inhomogeneous electric fields in compositionally-specific locations within the assembly, e.g., to enhance molecular detection sensitivity, plasmon-driven chemistry, or non-linear optical effects.

Though the present work focuses on optical extinction and transmission, MPM can be extended to address related properties of interest. One example is treating circularly polarized electric fields, enabling simulation and design of plasmonic materials with chiroptical responses.[21,47] Here we have established MPM's ability to quantify many-body contributions to the optical response of complex assemblies, treated at the level of dipoles. This approach explicitly incorporates structural complexity, explaining and predicting optical phenomena that cannot be captured in effective medium and mean field theories. Though many-bodied dipoles are sufficient to describe most observations of nanoparticle assemblies, it is possible, though increasingly computationally intensive, to make MPM more quantitatively predictive by systematically including higher-order polarization moments (quadrupoles, etc.) in the analysis. Finally, strategies for treating nonspherical nanoparticles have been developed as extensions to Mie theory,[14] and similar approaches may be pursued to extend MPM to handle triaxial

13

ellipsoids or cubes.

Methods

Synthesis and characterization of ITO nanocrystals. ITO nanocrystals were synthesized via established colloidal methods.[26,27] The size of the nanocrystals was extracted either from a spheroid fit of the SAXS pattern of a dilute nanocrystal dispersion (Fig. S12) or from statistics in bright-field scanning transmission electron microscope (STEM) or scanning electron microscopy (SEM) images (Fig. S6). STEM and SEM images were collected using a Hitachi S5500 on carbon support films on copper grids and Si substrates, respectively. The Sn atomic doping concentration was determined by Inductively Coupled Plasma-Optical Emission Spectrometry (ICP-OES) using a Varian 720-ES instrument following acid digestion. Dielectric functions were extracted by fitting to the heterogeneous Drude approximation model, which accounts for surface depletion and heterogeneity among the nanocrystal ensemble.[44] Fitting was based on optical transmission spectra (see below) collected on dilute nanocrystal dispersions with concentration determined using ICP-OES.

Mixed ITO nanocrystal superlattice assembly. ITO nanocrystal superlattices were formed by a liquid-air interface assembly method. After cleaning a $2\,\mathrm{cm} \times 2\,\mathrm{cm}$ Si substrate with Hellmanex ($2\,\mathrm{wt\%}$) and acetone solution, $250\,\mu\mathrm{L}$ of water was dropped on the substrate. On top of the water droplet, $100\,\mu\mathrm{L}$ of nanocrystal dispersion was dropped. Nanocrystals were dispersed in the 2:1 mixture of hexane and toluene with the addition of $5\,\mu\mathrm{L}$ of oleic acid. The amount of 1% Sn and 6% Sn ITO nanocrystals were adjusted to the desired mixing ratio while maintaining the total nanocrystal concentration in the solution at $1\,\mathrm{mg/mL}$. After depositing the nanocrystal dispersion, the substrate was partially covered with a glass slide to control the evaporation rate and convection flow. After evaporation of the solvent, the substrate was dried in air.

Gelation of AL-functionalized ITO nanocrystals. Aldehyde-terminated ligand (AL) was synthesized via previously reported synthetic protocols.[26] ITO nanocrys-

14

tals were functionalized by AL via a direct ligand exchange (Fig. S10), dispersed in N,N-dimethylformamide (DMF), and mixed with oxalyldihydrazide in ethylene glycol and TBAPF$_6$ in DMF to induce assembly. Gel structures were characterized by SAXS of capillaries measured in transmission using a SAXSLAB Ganesha; a dilute dispersion of nanocrystals was measured to record the form factor used in computing S for the gels (Fig. S12).

Optical measurements. For gels, the freshly prepared mixtures of AL-functionalized ITO nanocrystals and organics were injected into home-made glass sandwich cells with 25-micron-thick thermoplastic spacer and sealed with Kapton film (Fig. S17). Extinction spectra of both gels and superlattices were measured in transmission using an Agilent Cary 5000 for near-infrared and a Bruker Vertex 70 FTIR for mid-infrared.

Mutual polarization simulations. MPM simulations were performed in MAT-LAB using in-house code freely available at github.com/zeesherman/mutual-polarization. These simulations use a system of dimensionless units where $a = 1$, $\varepsilon_m = 1$, and $E_0 = 1$. For each frequency ω, the nanoparticle permittivity was set to $\varepsilon_p(\omega)$ and the N particle induced dipoles $\mathbf{p}_{ij}$ were computed for a particular field polarization $\mathbf{E}_0 = E_0\hat{\mathbf{e}}_j$ $(i = 1, \ldots, N, j = x, y, z)$ by solving eq 1 using GMRES with a relative error tolerance of 10^{-3}. During each iteration, the right side of eq 1 is evaluated to an absolute error tolerance of 10^{-3} using an Ewald summation procedure discussed in Supporting Information Sec. 1.2 and Ref. 39. The polarization-averaged extinction cross-section per nanoparticle volume is $\sigma = \sum_j \sigma_j/N_E$, where $\sigma_j = \frac{3\sqrt{\mu_m}\omega}{4\pi a^3 \sqrt{\varepsilon_m} E_0^2} \text{Im}[\sum_i \mathbf{p}_{ij} \cdot \mathbf{E}_0/N]$ and N_E is the number of field polarizations. The electric field at any point and other quantities are also computed from $\mathbf{p}_{ij}$ as detailed in Supporting Information Sec. 1.2. All dielectric functions used in this work are summarized in Table S3. σ in Fig. 1c was averaged over three polarizations and 20 equilibrated hard sphere configurations of $N = 8000$ from the Brownian dynamics method in Supporting Information Sec. 4.3.

Simulation of mixed nanocrystal superlattices. $N = 11600$ spherical nanoparticles of radius a were placed on a two-dimensional hexagonal lattice of area fraction 0.87 on the $z = 0$ plane inside a triply-periodic box, with a length of $50a$

in the z-direction normal to the lattice plane. Particles were randomly assigned to one of two %Sn dopant concentrations in proportion to the intended mixing fraction, with simple Drude dielectric functions described in Table S3. Two MPM simulations were performed for $\mathbf{E}_0 = E_0 \hat{\mathbf{e}}_j$ ($j = x, y$). The average dipole for each polarization was then computed $\langle \mathbf{p}_j \rangle = \sum_i \mathbf{p}_{ij}/N = \langle p_j \rangle \mathbf{e}_j$ and averaged over field polarizations $\langle p \rangle = (\langle p_x \rangle + \langle p_y \rangle)/2$. This process was repeated and $\langle p \rangle$ averaged over a total of 20 independently prepared lattices. The fraction of incident light transmitted T for the superlattices when placed on a $500\,\mu$m thickness silicon substrate is then computed from $\langle p \rangle$ through the procedure described in Supporting Information Sec. 4.2 and extinction reported as $-\log T$.

Simulation of nanocrystal gels. Brownian dynamics simulations were performed in HOOMD-blue (v2.9.7)[48] with $N = 64000$ spherical nanoparticles of mean thermodynamic radius $a = 7.32\,$nm, polydispersity of $0.10a$, and volume fraction of $\eta = 0.01$ in a triply-periodic box with an integration time step of $\Delta t = 10^{-4}\tau_D$, where $\tau_D = \gamma^H a^2/k_B T$ is the diffusion time in terms of the hydrodynamic drag coefficient γ^H. Nanoparticles interacted with hard sphere repulsions and short-ranged attractions of approximate range $0.1a$ and contact strength $10k_B T$. Three MPM simulations for each sampled configuration were performed to find the polarization-averaged extinction cross-section using an optical radius of $5.9\,$nm for all nanoparticles and a core-shell Drude dielectric function described in Table S3. The extinction spectra were normalized by dividing by their maximum values.

Acknowledgement

Supporting Information Available

Additional details of the mutual polarization method, nanocrystal synthesis and assembly, materials characterization, and other simulation aspects.

References

(1) Elghanian, R.; Storhoff, J. J.; Mucic, R. C.; Letsinger, R. L.; Mirkin, C. A. Selective colorimetric detection of polynucleotides based on the distance-dependent optical properties of gold nanoparticles. *Science* **1997**, *277*, 1078–1081.

(2) Le, F.; Brandl, D. W.; Urzhumov, Y. A.; Wang, H.; Kundu, J.; Halas, N. J.; Aizpurua, J.; Nordlander, P. Metallic nanoparticle arrays: a common substrate for both surface-enhanced Raman scattering and surface-enhanced infrared absorption. *ACS Nano* **2008**, *2*, 707–718.

(3) Atwater, H. A.; Polman, A. Plasmonics for Improved Photovoltaic Devices. *Nat. Mater.* **2010**, *9*, 205–2013.

(4) Liu, Z.; Hou, W.; Pavaskar, P.; Aykol, M.; Cronin, S. B. Plasmon resonant enhancement of photocatalytic water splitting under visible illumination. *Nano Lett.* **2011**, *11*, 1111–1116.

(5) Aslam, U.; Rao, V. G.; Chavez, S.; Linic, S. Catalytic Conversion of Solar to Chemical Energy on Plasmonic Metal Nanostructures. *Nat. Catal.* **2018**, *1*, 656–665.

(6) Lin, J.; Wang, S.; Huang, P.; Wang, Z.; Chen, S.; Niu, G.; Li, W.; He, J.; Cui, D.; Lu, G.; Chen, X.; Nie, Z. Photosensitizer-loaded gold vesicles with strong plasmonic coupling effect for imaging-guided photothermal/photodynamic therapy. *ACS Nano* **2013**, *7*, 5320–5329.

(7) Wang, S. et al. Plasmonic Copper Sulfide Nanocrystals Exhibiting Near-Infrared Photothermal and Photodynamic Therapeutic Effects. *ACS Nano* **2015**, *9*, 1788–1800.

(8) Giannini, V.; Fermández-Domínguez, A. I.; Heck, S. C.; Maier, S. A. Plasmonic Nanoatennas: Fundamentals and Their Use in Controlling the Radiative Properties of Nanoemitters. *Chem. Rev.* **2011**, *111*, 3888–3912.

(9) Agrawal, A.; Cho, S. H.; Zandi, O.; Ghosh, S.; Johns, R. W.; Milliron, D. J. Localized Surface Plasmon Resonance in Semiconductor Nanocrystals. *Chem. Rev.* **2018**, *118*, 3121–3207.

(10) Jain, P. K.; El-Sayed, M. A. Plasmonic coupling in noble metal nanostructures. *Chem. Phys. Lett.* **2010**, *487*, 153–164.

(11) Halas, N. J.; Lal, S.; Chang, W.-S.; Link, S.; Nordlander, P. Plasmons in strongly coupled metallic nanostructures. *Chem. Rev.* **2011**, *111*, 3913–3961.

(12) Ross, M. B.; Mirkin, C. A.; Schatz, G. C. Optical properties of one-, two-, and three-dimensional arrays of plasmonic nanostructures. *J. Phys. Chem. C* **2016**, *120*, 816–830.

(13) Pastoriza-Santos, I.; Kinnear, C.; Pérez-Juste, J.; Mulvaney, P.; Liz-Marzán, L. M. Plasmonic polymer nanocomposites. *Nat. Rev. Mater.* **2018**, *3*, 375–391.

(14) Quinten, M. *Optical properties of nanoparticle systems: Mie and beyond*, 1st ed.; Wiley-VCH: Weinheim, 2011.

(15) Prodan, E.; Radloff, C.; Halas, N. J.; Nordlander, P. A hybridization model for the plasmon response of complex nanostructures. *Science* **2003**, *302*, 419–422.

(16) Storhoff, J. J.; Lazarides, A. A.; Mucic, R. C.; Mirkin, C. A.; Letsinger, R. L.; Schatz, G. C. What controls the optical properties of DNA-linked gold nanoparticle assemblies? *J. Am. Chem. Soc.* **2000**, *122*, 4640–4650.

(17) Lazarides, A. A.; Schatz, G. C. DNA-linked metal nanosphere materials: Structural basis for the optical properties. *J. Phys. Chem. B* **2000**, *104*, 460–467.

(18) Ghosh, S. K.; Pal, T. Interparticle Coupling Effect on the Surface Plasmon Resonance of Gold Nanoparticles: From Theory to Applications. *Chem. Rev.* **2007**, *107*, 4797–4862.

(19) Myroshnychenko, V.; Rodríguez-Fernández, J.; Pastoriza-Santos, I.; Funston, A. M.; Novo, C.; Mulvaney, P.; Liz-Marzán, L. M.; De Abajo, F. J. G. Modelling the optical response of gold nanoparticles. *Chem. Soc. Rev.* **2008**, *37*, 1792–1805.

(20) Wriedt, T. Light scattering theories and computer codes. *J. Quant. Spectrosc. Radiat. Transf.* **2009**, *110*, 833–843.

(21) Fan, Z.; Govorov, A. O. Plasmonic Circular Dichroism of Chiral Metal Nanoparticle Assemblies. *Nano Lett.* **2010**, *10*, 2580–2597.

(22) Cargnello, M.; Johnston-Peck, A. C.; Diroll, B. T.; Wong, E.; Datta, B.; Damodhar, D.; Doan-Nguyen, V. V. T.; Herzing, A. A.; Kagan, C. R.; Murray, C. B. Substitutional Doping in Nanocrystal Superlattices. *Nature* **2015**, *524*, 450–453.

(23) Shi, Q.; Sikdar, D.; Fu, R.; Si, K. J.; Dong, D.; Liu, Y.; Premaratne, M.; Cheng, W. 2D Binary Plasmonic Nanoassemblies with Semiconductor n/p-Doping-Like Properties. *Adv. Mater.* **2018**, *30*, 1801118.

19

(24) Jishkariani, D.; Elbert, K. C.; Wu, Y.; Lee, J. D.; Hermes, M.; Wang, D.; van Blaaderen, A.; Murray, C. B. Nanocrystal Core Size and Shape Substitutional Doping and Underlying Crystalline Order in Nanocrystal Superlattices. *ACS Nano* **2019**, *13*, 5712–5719.

(25) Saez Cabezas, C. A.; Ong, G. K.; Jadrich, R. B.; Lindquist, B. A.; Agrawal, A.; Truskett, T. M.; Milliron, D. J. Gelation of Plasmonic Metal Oxide Nanocrystals by Polymer-Induced Depletion Attractions. *Proc. Natl. Acad. Sci. U.S.A.* **2018**, *115*, 8925–8930.

(26) Dominguez, M. N. et al. Assembly of Linked Nanocrystal Colloids by Reversible Covalent Bonds. *Chem. Mater.* **2020**, *32*, 10234–10245.

(27) Kang, J.; Valenzuela, S. A.; Lin, E. Y.; Dominguez, M. N.; Sherman, Z. M.; Truskett, T. M.; Anslyn, E. V.; Milliron, D. J. Colorimetric Quantification of Linking in Thermoreversible Nanocrystal Gel Assemblies. *Sci. Adv.* **2022**, *8*, eabm7364.

(28) Kodanek, T.; Freytag, A.; Schlosser, A.; Naskar, S.; Härtling, T.; Dorfs, D.; Bigall, N. C. Macroscopic Aerogels with Retained Nanoscopic Plasmonic Properties. *Z. Phys. Chem.* **2018**, *232*, 1675–1689.

(29) Wen, D.; Liu, D., Wen znd Haubold; Zhu, C.; Oschatz, M.; Holzschuh, M.; Wolf, A.; Simon, F.; Kaskel, S.; Eychmüller, A. Gold Aerogels: Three-Dimensional Assembly of Nanoparticles and Their Use as Electrocatalytic Interfaces. *ACS Nano* **2016**, *10*, 2559–2567.

(30) Fuller, K. A. Optical resonances and two-sphere systems. *Appl. Opt.* **1991**, *30*, 4716–4731.

(31) Mackowski, D. W.; Mishchenko, M. I. Calculation of the T matrix and the scattering matrix for ensembles of spheres. *J Opt. Soc. Am. A* **1996**, *13*, 2266–2278.

(32) Mackowski, D. W.; Mishchenko, M. I. A multiple sphere T-matrix Fortran code for use on parallel computer clusters. *J. Quant. Spectrosc. Radiat. Transf.* **2011**, *112*, 2182–2192.

(33) Egel, A.; Pattelli, L.; Mazzamuto, G.; Wiersma, D. S.; Lemmer, U. CELES: CUDA-accelerated simulation of electromagnetic scattering by large ensembles of spheres. *J. Quant. Spectrosc. Radiat. Transf.* **2017**, *199*, 103–110.

(34) Patteli, L.; Egel, A.; Lemmer, U.; Wiersma, D. Role of Packing Density and Spatial Correlations in Strongly Scattering 3D Systems. *Optica* **2018**, *5*, 1037–1045.

(35) Rotne, J.; Prager, S. Variational treatment of hydrodynamic interaction in polymers. *J. Chem. Phys.* **1969**, *50*, 4831–4837.

(36) Fiore, A. M.; Balboa Usabiaga, F.; Donev, A.; Swan, J. W. Rapid sampling of stochastic displacements in Brownian dynamics simulations. *J. Chem. Phys.* **2017**, *146*, 124116.

(37) Keaveny, E. E.; Maxey, M. R. Modeling the magnetic interactions between paramagnetic beads in magnetorheological fluids. *J. Comput. Phys.* **2008**, *227*, 9554–9571.

(38) Sherman, Z. M.; Ghosh, D.; Swan, J. W. Field-directed self-assembly of mutually polarizable nanoparticles. *Langmuir* **2018**, *34*, 7117–7134.

(39) Lindbo, D.; Tornberg, A.-K. Spectral Accuracy in Fast Ewald-based Methods for Particle Simulations. *J. Comput. Phys.* **2011**, *230*, 8744–8761.

(40) Saad, Y.; Schultz, M. H. GMRES: A generalized minimal residual algorithm for solving nonsymmetric linear systems. *SIAM J. Sci. Statist. Comput.* **1986**, *7*, 856–869.

(41) Schevchenko, E. V.; Talapin, D. V.; Kotov, N. A.; O'Brien, S.; Murray, C. B. Structural Diversity in Binary Nanoparticle Superlattices. *Nature* **2006**, *439*, 55–59.

(42) Young, K. L.; Ross, M. B.; Blaber, M. G.; Rycenga, M.; Jones, M. R.; Zhang, C.; Senesi, A. J.; Lee, B.; Schatz, G. C.; Mirkin, C. A. Using DNA to design plasmonic metamaterials with tunable optical properties. *Adv. Mater.* **2014**, *26*, 653–659.

(43) Schimpf, A. M.; Lounis, S. D.; Runnerstrom, E. L.; Milliron, D. J.; Gamelin, D. R. Redox chemistries and plasmon energies of photodoped In_2O_3 and Sn-doped In_2O_3 (ITO) nanocrystals. *J. Am. Chem. Soc.* **2015**, *137*, 518–524.

(44) Gibbs, S. L.; Staller, C. M.; Agrawal, A.; Johns, R. W.; Saez Cabezas, C. A.; Milliron, D. J. Intrinsic Optical and Electronic Properties from Quantitative Analysis of Plasmonic Semiconductor Nanocrystal Ensemble Optical Extinction. *J. Phys. Chem. C* **2020**, *124*, 24351–24360.

(45) Del Gado, E.; Kob, W. Structure and relaxation dynamics of a colloidal gel. *Europhys. Lett.* **2005**, *72*, 1032–1038.

(46) Sherman, Z. M.; Howard, M. P.; Lindquist, B. A.; Jadrich, R. B.; Truskett, T. M. Inverse methods for design of soft materials. *J. Chem. Phys.* **2020**, *152*, 140902.

(47) Kim, Y.; Yeom, B.; Arteaga, O.; Yoo, S. J.; Lee, S.-G.; Kim, J.-G.; Kotov, N. A. Reconfigurable chiroptical nanocomposites with chirality transfer from the macro- to the nanoscale. *Nat. Mater.* **2016**, *15*, 461–468.

(48) Anderson, J. A.; Glaser, J.; Glotzer, S. C. HOOMD-blue: A Python Package for High-Performance Molecular Dynamics and Hard Particle Monte Carlo Simulations. *Comput. Mater. Sci* **2020**, *173*, 109363.

Graphical TOC Entry